

Long-Chain Lipids Facilitate Insertion of Large Nanoparticles into Membranes of Small Unilamellar Vesicles

Adan Marzouq,[¶] Lion Morgenstein,[¶] Carlos A. Huang-Zhu,[¶] Shimon Yudovich, Ayelet Atkins, Asaf Grupi,^{*} Reid C. Van Lehn,^{*} and Shimon Weiss^{*}



Cite This: *Langmuir* 2024, 40, 10477–10485



Read Online

ACCESS |



Metrics & More

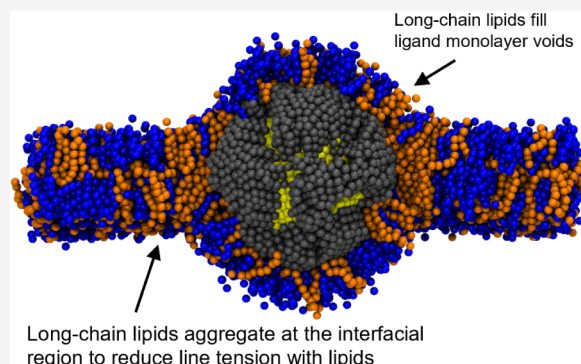


Article Recommendations



Supporting Information

ABSTRACT: Insertion of hydrophobic nanoparticles into phospholipid bilayers is limited to small particles that can incorporate into a hydrophobic membrane core between two lipid leaflets. Incorporation of nanoparticles above this size limit requires the development of challenging surface engineering methodologies. In principle, increasing the long-chain lipid component in the lipid mixture should facilitate incorporation of larger nanoparticles. Here, we explore the effect of incorporating very long phospholipids (C24:1) into small unilamellar vesicles on the membrane insertion efficiency of hydrophobic nanoparticles that are 5–11 nm in diameter. To this end, we improve an existing vesicle preparation protocol and utilized cryogenic electron microscopy imaging to examine the mode of interaction and evaluate the insertion efficiency of membrane-inserted nanoparticles. We also perform classical coarse-grained molecular dynamics simulations to identify changes in lipid membrane structural properties that may increase insertion efficiency. Our results indicate that long-chain lipids increase the insertion efficiency by preferentially accumulating near membrane-inserted nanoparticles to reduce the thermodynamically unfavorable disruption of the membrane.



INTRODUCTION

In recent years, synthesis methods for the production of high-quality nanoparticles (NPs) have greatly improved, allowing for increased control over their size, shape, and chemical and physical properties. This, in turn, enables the fabrication of sophisticated metallic, magnetic, dielectric, and semiconducting heterostructured NPs with desirable photophysical and chemical properties.^{1–4} This precise control allows the engineering of excited-state wave functions,^{5–7} charge confinement, and spatiotemporal control of charge-separated states.⁸ Hence, NPs (and in particular semiconducting NPs) have proved to be very useful in diverse applications such as in optoelectronics,^{9,10} biological imaging,¹¹ sensing,^{12–14} catalysis,¹⁵ energy harvesting,¹⁶ biomedicine, and cell surface engineering.^{17–20}

While these sophisticated inorganic nanomaterials require advanced synthesis methods, their integration with biological macromolecules and machineries requires additional functionalization steps. Current approaches typically target NPs to interact with the cell membrane's surface or to undergo cellular uptake. Less effort has been invested in the functionalization of NPs that could be targeted, incorporated into, and retained in the membrane bilayer core itself.²¹ Such membrane-inserted NPs could expand the repertoire of desired cellular functions while taking advantage of the superior inorganic materials' properties.^{22,23} Once inserted into the membrane, such NPs

could, for example, introduce orthogonal (to native signaling) ways to communicate with the cell's interior, introduce de novo or enhance native enzymatic/catalytic activities, sense the membrane potential, or be used as antennas for light harvesting and vision restoration.^{4,24,25}

The underlying obstacle for stable insertion of large NPs into lipid membranes is that in many cases, the surfaces of as-synthesized NPs are decorated with a mixture of highly hydrophobic ligands and are insoluble in biologically relevant aqueous media. Therefore, without any surface modification, these hydrophobic NPs must be efficiently incorporated into synthetic vesicle membranes between the two leaflets. Since phospholipid bilayers are typically 4–5 nm thick,^{26,27} successful membrane insertion has been achieved only for small NPs with sizes ≤ 5 nm.^{28–30} Inclusion of larger hydrophobic NPs is thermodynamically unfavorable due to the energetic penalty associated with the protrusion of hydrophobic ligands into the surrounding polar solvent³⁰ or due to the deformation of the bilayer to minimize such

Received: November 15, 2023

Revised: April 27, 2024

Accepted: April 29, 2024

Published: May 6, 2024



Table 1. Five Different Lipid Composition Used for the Liposome Studies with [PC24] Increasing from 0 mol % (Sample 1) to 100 mol % (Sample 5)

sample	composition			
	PC24 (mol %)	POPC (mol %)	CHOL (mol %)	DOTAP (mol %)
1	0	70	20	10
2	25	51	14	10
3	50	31	9	10
4	75	12	3	10
5	100	0	0	0

protrusion.^{31–33} This limitation practically excludes higher-order structures and functionalities that could be beneficial in terms of signal or actuation strength.

We hypothesized that the addition of long-chain lipids should promote the insertion of larger NPs than previously accomplished. The thickness of the phospholipid membrane can be increased by the incorporation of lipids with a long alkane chain and by the addition of cholesterol (CHOL), which aligns and stretches alkane chains into a packed and thick membrane.²⁶ To test this hypothesis, we prepared small unilamellar lipid vesicles incorporating 1,2-dinervonylsnglycero-3-phosphocholine (PC24), an unsaturated zwitterionic phospholipid with 24 carbon alkane chains. This lipid has been previously used in the preparation of multilamellar liposome (MLV) formulations with protein or peptide drugs, and in the formation of planar bilayer lipid membranes.³⁴ In biological systems, it is a component of lipid rafts and microdomains.³⁵

Compared to typical PC18 lipids, which form membranes of 4–5 nm thickness, lipid bilayers consisting of 25% PC24 are expected to lead to a 20% increase in membrane thickness, i.e., up to 6 nm. To test our hypothesis, we evaluated the membrane-insertion efficiency of inorganic NPs in the size range of 5–11 nm in diameter into the lipid bilayer of small unilamellar vesicles (SUVs) containing various molar fractions of PC24 during the formation of lipid vesicles. Initial attempts to incorporate even small NPs into SUVs prepared by the hydration method³⁶ were unsuccessful. After testing several other SUV preparation protocols for NP insertion that failed, we identified in the literature a protocol that was previously used to encapsulate hydrophobic drugs into liposomes' membranes³⁷ but never applied for membrane incorporation of nanoparticles. This approach proved to be highly efficient for the membrane insertion of small NPs. A critical step in this protocol is the addition of a lipid detergent to an organic solution containing both lipids and NPs. With the addition of PC24 to the lipid mixture,³⁴ we found that NPs with diameters of up to ~11 nm were successfully incorporated into SUV membranes.

Here, we present a detailed protocol for the incorporation of large NPs (up to ~11 nm in diameter) into the lipid membrane of SUVs with optimized lipid composition, detergent, organic solvents, and the NP/lipid ratio. Cryogenic electron microscopy (cryo-EM) imaging of these membrane-inserted NPs is used for the characterization of their mode of interaction with the membrane, indicating their insertion to the midplane of the membrane. To determine the role of PC24 in facilitating insertion, we further performed coarse-grained molecular dynamics simulations to interrogate the lipid structural organization around membrane-embedded NPs. The simulations show that the longer PC24 lipids accumulate near membrane-inserted NPs to reduce the degree of membrane disruption and minimize exposure of the hydro-

phobic area to solvent, thereby modulating the insertion efficiency of large NPs even without substantial changes in overall membrane thickness.

RESULTS AND DISCUSSION

In order to insert NPs efficiently into the lipid bilayer of SUVs, we adopted a detergent dialysis-based vesicle preparation method that was previously optimized for membrane incorporation of small hydrophobic drugs.³⁷ This procedure was modified to allow for the insertion of NPs into SUV membranes. Two different mixtures of lipids were used for SUV preparation: a “native membrane” mixture with POPC, CHOL, and DOTAP (central column in Table 1), and a “thick membrane” mixture with POPC, CHOL, DOTAP, and a very long-chain phospholipid (PC24). Insertion efficiency was tested for four different sizes of NPs: 5, 7, and 11 nm diameter spherical CdSe/ZnS quantum dots (QDs; sizes determined by TEM; Table S1). Cryo-EM imaging was used to assess the mode of NP interaction/insertion with/into the SUVs' membrane. As described in the Supporting Information, the yield of NP insertion into the membrane was evaluated by examining the cryo-EM images and counting membrane-inserted NPs, membrane-adsorbed NPs, and encapsulated NPs. We excluded all NPs that were either interacting with the carbon grid or aggregated. Multiple experiments on different days were conducted for each condition (NP size and “native” or “thick” membrane). Preparations were repeated for each condition, and multiple field-of-views (FOVs) were collected from each grid. Insertion efficiency was defined as the ratio between the number of membrane-inserted NPs and the total number of NPs in a frame. Results from all analyzed frames per condition were averaged. We note that the surfaces of the QDs are coated with hydrophobic ligands as prepared, facilitating their favorable interaction with the membrane core.

In order to find a suitable working concentration of PC24 to be added to the “thick membrane” mixture, we first tested five preparations of SUVs using different relative concentrations of PC24 and evaluated the effect of PC24 concentration (Table S2). SUVs were prepared as described in the Supporting Information. Each preparation was imaged by cryo-EM in order to assess the morphology and uniformity of different SUV composition. Based on cryo-EM imaging, we found that a relative molar concentration of [PC24] = 25 mol % resulted in relatively uniform and spherical SUVs, while concentrations above [PC24] = 25 mol % resulted in polygonal SUV formation, with SUVs' morphology being less spherical and more polygonal as [PC24] increased (Figure S2). Furthermore, [PC24] = 50% showed remarkably decreased SUV formation yields, and a negligible number of SUVs were observed via cryo-EM imaging. The nonspherical, polygonal SUV shapes can be attributed to the membrane's gel phase behavior, since PC24 has a transition temperature of 26

$^{\circ}\text{C}$,^{38–40} which is higher than the transition temperature of POPC (-2°C). Assuming uniform lipid mixing and distribution and given the transition temperature of each lipid component, it is reasonable to assert that using a high component fraction of PC24 lipids in the SUV composition, which were exposed in this work to room temperature prior to cryo-EM imaging, will result in solid/gel phase lipid bilayer behavior that will interfere with both spherical SUV formation and the incorporation of nanoparticles into the bilayer.

Figure 1 shows the cryo-EM images of selected examples of successful insertion of the different size/type of NPs into SUVs

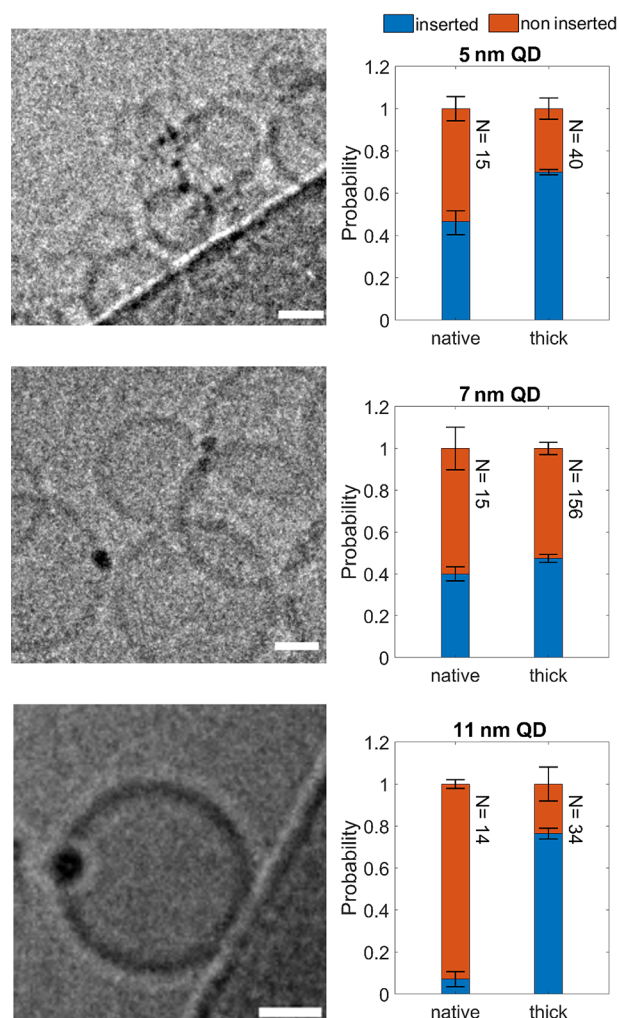


Figure 1. Incorporation of NPs into thick SUV membranes. Left column: cryo-EM images showing examples for insertion of 5, 7, and 11 nm QDs (from top to bottom) into thick SUV membranes. Right column: corresponding insertion efficiencies of NPs in native and thick membranes, while N is the total number of counted particles. Lipid composition for native and thick membranes is described in Table S2. Scale bars: 20 nm.

created from the “thick” membrane mixture. The morphologies of the SUVs at different PC24 concentrations are shown in Figure S2 and raw images are deposited.⁴⁰ The blue and red bars on the right columns indicate the fractions of inserted and noninserted particles, respectively, out of all counted particles, excluding aggregates and carbon-interacting particles.

As expected, insertion efficiency was inversely proportional to the NP size for native membranes due to the NP size,

whereas the long lipid addition had a significant effect on the larger particle as a result of the addition of long-chain lipids. Interestingly, while the insertion efficiency for the largest QDs (11 nm) was 7.1% in the native membrane lacking PC24, it increased to 76.5% when inserted into the “thick” membrane containing [PC24] = 25 mol %. For other NPs, we saw an increase from 46% to 70% for the 5 nm QDs and 40% to 48% for the 7 nm QDs.

We note the low number of observed membrane-inserted QDs, especially for the sample preparation conditions expected to have a lower incorporation yield, such as in the case of membranes lacking long-chain PC24 lipids. Observing membrane incorporation in such low-yield samples via cryo-EM imaging, which has an inherently low throughput, is challenging in terms of attaining statistically significant data. However, our observations provide strong evidence of the increased insertion efficiency of large quantum dots into PC24-containing vesicles. This evidence is most significant for 11 nm QDs, where membrane incorporation is essentially unattainable for “thin” membranes, and does occur for “thick” PC24-containing vesicles. In addition, while the ratio between inserted and noninserted 7 nm QDs in “native” and “thick” membranes is similar, it is worth noting that the total number of both inserted and noninserted 7 nm QDs was significantly higher for the case of “thick” PC24-containing vesicles. The higher number of SUVs associated with QDs can indicate that while full membrane insertion of 7 nm QDs is not more stable with the presence of PC24 lipids, their transient incorporation is more likely, resulting in a higher frequency of SUVs interacting with QDs at the moment of sample plunge freezing.

We further evaluated the degree of insertion for the 11 nm QDs by localizing the position of QDs relative to the SUVs’ membranes using home-written software, as described in the Supporting Information. Figure 2d shows a histogram of these

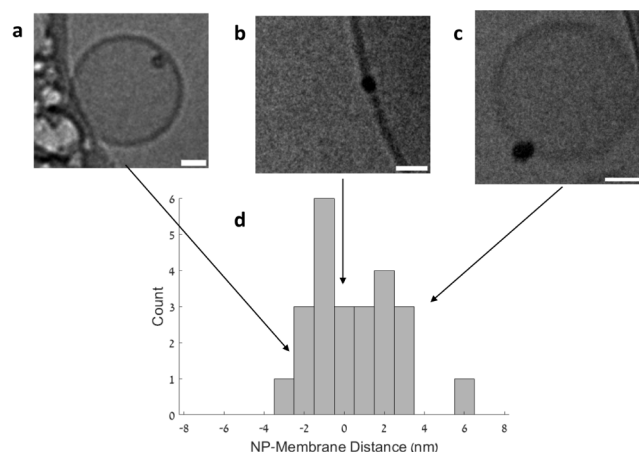


Figure 2. (a–c) Cryo-EM images showing 11 nm QDs inserted into thick SUVs. (d) Position distribution of QDs interacting with thick membrane SUVs. Only QDs that were in the vicinity of an SUV, but not in the vicinity of other QDs, were counted (24 QDs in total). Scale bars: 20 nm.

distances: positive distances represent locations in the outer SUV leaflet and outward from center of the SUV, and negative distances represent locations in the inner SUV leaflet and inward toward the center of the SUV. The histogram shows that these large NPs are most likely to be located near the center of the membrane. Figure 2a–c shows three examples of

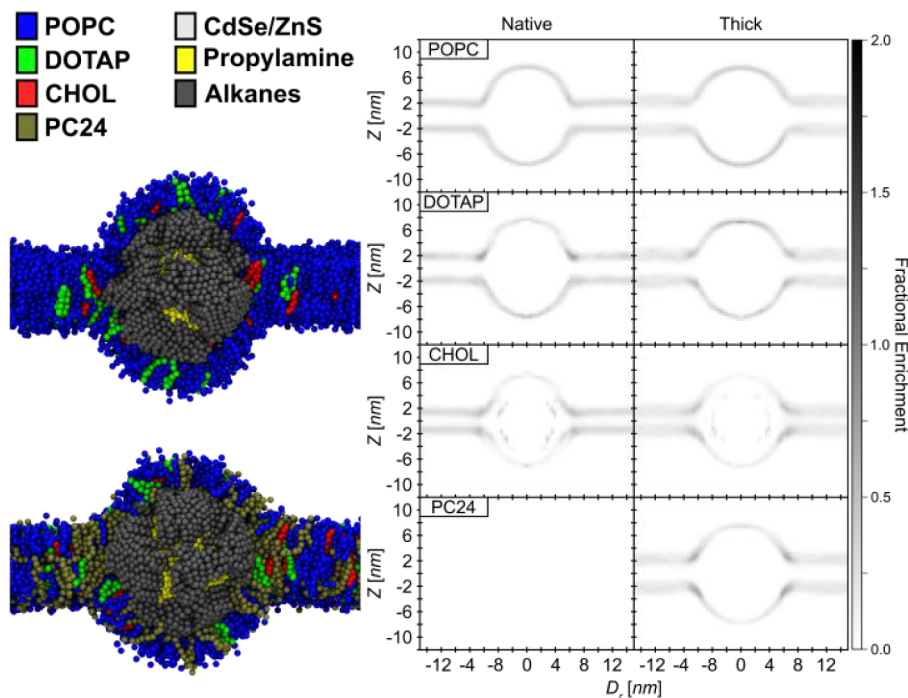


Figure 3. Simulation snapshots and 2D histograms of lipid headgroups for the 7 nm QD. Snapshots show the side view of the inserted QD with all water molecules, counterions, and half of the lipids in the y -axis with respect to the center of mass of the QD removed for visual purposes. The native membrane is shown at the top and thick membrane at the bottom. For the 2D histograms, Z is the distance along the z -axis, and D_r is the radial distance from the center of the QD in the xy -plane. The lipid headgroups selected for analysis were the phosphate group for POPC and PC24, the choline group for DOTAP, and the hydroxyl group for CHOL; they were binned radially in 0.375 nm wide by 0.375 nm tall bins and normalized by the volume of each bin and the number of configurations sampled. The color bar represents the fractional enrichment defined as the volumetric density of the lipid headgroups (lipids/nm³) normalized by the volumetric density of the lipid headgroups in the corresponding pure bilayer system.

analyzed FOVs, representing QDs that are located inward the SUV, the bilayer midline, and outward the SUV, respectively.

We next performed molecular dynamics simulations to simulate the spherical QDs in their membrane-inserted states and characterize the role of PC24 in modulating lipid organization and structural properties to promote insertion efficiency. Due to the large size of these systems, we performed coarse-grained molecular dynamics simulations using the MARTINI⁴¹ force field, version 2.3P,^{42,43} with the refined polarizable water model,⁴⁴ see the [Materials and Methods](#) section for molecular dynamics simulations. Details on the CG models, simulation parameters, and simulation convergence are included in the [Supporting Information](#) (Tables S3–S5 and Figures S4,S5). Since the same trends were observed across the three QDs, we only show data for the intermediate 7 nm QD here; data for the 5 and 11 nm QDs are included in [Figures S10–S16](#).

Figure 3 shows snapshots of final configurations of the 7 nm QDs in the native and thick membranes. The accompanying histograms show the volumetric density of headgroups (lipids/nm³) for each lipid species normalized by the volumetric density of the same headgroups in a bilayer without the inserted QD. These histograms provide information about the enrichment of each species compared to the bulk bilayer. Several observations are apparent from these data. First, comparing the POPC histograms at radial distances far from the QD reveals no significant increase in the average bilayer thickness in the thick membrane compared to the native membrane, likely because the fraction of PC24 (25 mol %) is

small compared to POPC (45 mol %). Second, lipids extract from the membrane and onto the surface of the QD to shield the hydrophobic QD surface and ligands from water. At equilibrium, the inserted QDs are fully enveloped by lipids, in agreement with similar reports in the literature.^{45,46} This behavior leads to substantial deformation of the extracted lipids due to the high curvature of the NP surface, which is expected to be unfavorable. Third, the simulation snapshots demonstrate the formation of bundles of hydrophobic ligands with voids between bundles;⁴⁷ these voids are filled with lipid tails (not visible in [Figure 3](#) but shown in [Figures S17–S19](#)).

A key distinction between the native and thick membranes is that PC24 is enriched in the region near the QD in the thick membranes (observed from the dark color for PC24 in [Figure 3](#)). This preferential enrichment results in an interfacial region around the QD that has a different lipid composition than that of the bulk bilayer. We further quantified enrichment by computing the area density of lipids (lipids/nm²) at fixed radial distances from the center of the QD. [Figure 4a,b](#) reveals peaks in these area densities that corroborate the lipid enrichment and depletion at defined radial distances. Specifically, in both the native and thick membranes the POPC and DOTAP densities are maximized at a radial distance of 5–7 nm from the center of the QD, which we define as the QD-membrane interfacial region. We also observed that in thick membranes the area density for POPC and DOTAP decreases in this interfacial region while the area density of PC24 increases. Both observations are in agreement with their corresponding 2D histograms in [Figure 3](#) and indicate that PC24

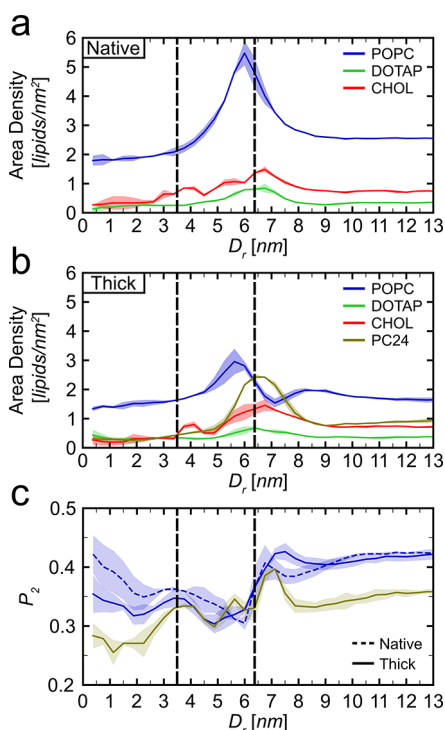


Figure 4. Lipid properties were computed for the 7 nm QD. D_r is the radial distance from the center of the QD in the xy -plane, and parameters are calculated in radial bins with a width of 0.375 nm. The lipid headgroups selected for analysis were the phosphate group for POPC and PC24, the choline group for DOTAP, and the hydroxyl group for CHOL lipid area density (lipids/nm²) for each type of lipid in the native (A) and thick (B) membranes. (C) Lipid tail order parameter, P_2 , computed for POPC and PC24 in both native and thick membranes. The left vertical dashed line corresponds to the QD radius, and the right vertical dashed line corresponds to the radial distance corresponding to the maximum area density of PC24. The error was calculated as the standard deviation between the two replicas.

preferentially accumulates in the QD-membrane interfacial region, primarily displacing POPC.

We hypothesized that the preferential enrichment of PC24 lipids in the QD-membrane interfacial region could stabilize QD insertion by reducing the extent of bilayer disruption. To test this hypothesis, we computed the P_2 lipid tail order parameter of the lipid acyl chain tails,⁴⁸ which is defined as

$$P_2 = \frac{1}{2} \langle 3 \cos^2 \theta - 1 \rangle$$

where θ denotes the angle between the vector connecting two consecutive lipid tail beads and the local vector normal to the monolayer containing that lipid. For each lipid, P_2 was computed for vectors connecting every consecutive tail bead (from the last hydrophobic bead to the glycerol bead). Details on how the local normal vectors and P_2 were computed are included in the [Supporting Information](#). This parameter measures the structural orientation between consecutive tail beads with respect to the local bilayer normal; aligned lipid tails increase the P_2 , indicating increased tail order. [Figure 4c](#) compares values of P_2 (reported as an average over values of P_2 computed for all consecutive tail bead vectors in both tails) for lipids near the QD to values of P_2 for lipids far from the QD in both the native and thick membranes to quantify QD-driven membrane disruption (indicated by lower values of P_2). [Figure](#)

4c shows that compared to its bulk value in the native membrane, P_2 substantially decreases for the POPC lipids in the QD-membrane interfacial region where the area density of POPC reaches a maximum ([Figure 4a](#)). This observation is consistent with the energetically unfavorable disruption of the lipid order in this interfacial region due to the presence of the QD. P_2 increases for lipids extracted onto the QD to achieve values similar to those of the bulk values. Similar behavior is observed for POPC in the thick membrane. Conversely, for the long-chain PC24 lipids, P_2 peaks near its density maximum but then decreases to a lesser degree in the QD-membrane interfacial region relative to values of P_2 in the bulk. The similarity of P_2 to the bulk value indicates less disruption of these lipids compared with the shorter-chain POPC lipids.

We further computed P_2 values as a function of tail bead number for all consecutive tail beads in the CG simulations, which we refer to as segmental P_2 values ([Figure S8](#)). Comparing segmental P_2 values for lipids in the QD-membrane interfacial region to lipids in the bulk again confirms that POPC lipids exhibit decreased ordering consistent with membrane disruption in both native and thick membranes but disruption occurs to a lesser extent in the thick membrane. Moreover, PC24 shows almost no change in the lipid tail order between bulk and interface lipids, further suggesting that long-chain lipids effectively decrease membrane disruption to allow higher NP insertion efficiency. Together, the data in [Figures 4](#) and [S8](#) indicate that in the thick membrane PC24 lipids preferentially accumulate in the QD-membrane interfacial region to reduce overall membrane disruption compared with the native membrane.

A second distinction between the native and thick membranes relates to the voids between ligand bundles observable in [Figure 4](#); these voids are filled with lipid tails to minimize contact between hydrophobic ligand backbones and water. In the thick membrane, PC24 lipids preferentially partition into these void regions and exclude POPC lipids ([Figures S17–S19](#)), similar to the exclusion of POPC lipids from the QD-membrane interfacial region. These results suggest that the PC24 tails can more favorably partition into the void spaces given their longer length than the POPC tails, providing another mechanism to minimize overall bilayer disruption in the thick membranes.

Previous works have shown that only very small QDs (<4 nm)^{27–29} can be incorporated into SUV membranes during their formation using electro-swelling, sonication, and other detergent removal protocols.³⁷ Here, we used a different approach that relied on a previously published protocol for membrane incorporation of small hydrophobic drug molecules.³³ In this approach, a dialysis-based detergent removal step was performed during the preparation of the vesicles. This improved protocol was sufficient for the insertion of larger (>5 nm) particles into SUVs with membranes composed of POPC and CHOL, although at low efficiency. The addition of 25 mol % of a long-chain phospholipid, PC24, significantly improved the insertion of large particles into SUV membranes, and facilitated the insertion of large QDs (~11 nm) at high efficiency. Combining both approaches, NPs as large as 11 nm QDs were successfully inserted into SUVs.

Coarse-grained molecular simulations suggest two key factors for why long-chain lipids facilitate the insertion of large CdSe/ZnS QDs coated with octadecylamine ligands, as schematically illustrated in [Figure 5](#). First, long-chain lipids preferentially accumulate in the interfacial region at the QD-

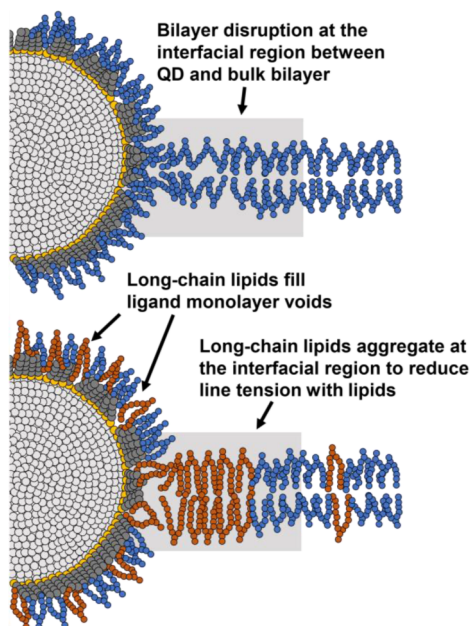


Figure 5. Schematic illustration of the long-chain lipid aggregation and increased lipid tail order in the interfacial region between the QD and the bulk bilayer (shaded region). Long-chain lipids (PC24) are colored orange. Medium-chain lipids (POPC and DOTAP) are colored blue. The QD shell is colored light gray, the amine group of the ligands are colored yellow, and the ligand hydrophobic groups are colored gray.

membrane interface, displacing POPC. The thicker interfacial region results in less disruption of the bilayer compared to that of the native membrane, which is energetically favorable and thermodynamically stabilizes QD insertion. PC24 thus acts similarly to a linactant,⁴⁹ a molecule that decreases the line tension between lipid domains. In this case, the line tension at the interface between lipids on the QD and lipids on the bulk bilayer is decreased, potentially increasing insertion efficiency for large NPs. Second, PC24 preferentially fills voids in the ligand monolayer that arise due to the formation of ligand bundles, again displacing POPC. The longer PC24 tails can more effectively pack against the long octadecylamine ligand backbones to again minimize bilayer disruption. These factors point to PC24-induced changes to lipid structural organization as facilitating QD insertion, even without substantial changes in the overall membrane thickness.

CONCLUSION

In summary, we developed a lipid composition and SUV preparation protocol that promotes the integration of large inorganic hydrophobic particles into membranes. It is well-accepted that membrane thickness varies with acyl chain length and the presence of cholesterol. We found that adding long-chain phospholipids (C24:1) to the vesicle formulation is crucial for the incorporation of NPs with diameters much larger than those reported for typical lipid composition. Molecular dynamics simulations indicate that the long-chain lipids act like linactants that stabilize membrane-inserted QDs. Although the main obstacle for NP incorporation into SUVs is their size, the effect of the hydrophobic capping ligand layer and the particle geometry on insertion into SUVs is a matter of future study. These SUVs could be made fusogenic to allow the delivery of NPs into the cellular membranes. The

technology developed here could be applied to diagnostic technologies, therapeutic applications, and as a research tool for studying membrane properties. The computational approach in this work can also be potentially applied to other classes of nanomaterials and more biologically relevant membrane models to analyze the insertion efficiency. By enabling these predictions, we can explore a wider range of materials as biomedical agents.

MATERIALS AND METHODS

Chemicals. All chemicals of the highest purity available were purchased and were used without further purifications; buffer solutions and sodium cholate were purchased from Sigma-Aldrich. 1-Palmitoyl-2-oleoyl-glycero-3-phosphocholine (POPC), 1,2-dioleoyl-3-trimethylammonium-propane (chloride salt) (DOTAP), cholesterol, and 1,2-dinervonoylsn-glycero-3-phosphocholine (PC24) were purchased from Avanti Polar Lipids. The as-synthesized 5 nm QDs were purchased from Cytodiagnostics (Burlington, Canada), and 7 and 11 nm QDs were purchased from ocean nanotech (San Diego, USA).

TEM Imaging. Carbon type A grid (Ted Pella Inc., Redding, USA) was glow discharged with a EmiTech K100 machine (Emitech Group, France), and then 3 μL of NP was loaded on the grid. After 1 min the sample was blotted and access material was removed then air-dried. The sample was then inspected with a Tecnai G2 microscope (FEI, Teramo fisher, Massachusetts, USA) with an acceleration voltage of 120 kV. Images were taken using Digital Micrograph with a MultiScan Camera model 794 (Gatan, Inc., Pleasanton, United States) in different resolutions.

Absorbance Spectroscopy. The absorbance spectra of NPs were obtained with an Ocean Optics USB4000 spectrophotometer (Ostfildern, Germany). The spectra of NPs were obtained at a scan rate of 1200 nm/min with a 1 cm path length in a quartz cuvette.

Preparation of NP Embedded SUVs. In a typical preparation of SUV/NP constructs, 7 μmol of total lipids (Table 1) were mixed with NPs (10 μL of 5 μM stock solution in chloroform) and dissolved in 30 μL methanol:methylene chloride:chloroform (1:1:1; v:v:v). Next, 13 mg of the detergent sodium cholate was added to the organic solution giving 50 mM final concentration. In the next step, the organic solutions were evaporated for 1 h at 45 $^{\circ}\text{C}$ using a vacuum evaporator. Afterward, the dry film was resuspended with 0.5 mL of 20 mM phosphate buffer pH 7.2, giving the final lipid concentration of 18 mM, and the solution was equilibrated at 45 $^{\circ}\text{C}$ for 1 h.

Detergent was removed by controlled dialysis of the mixture against 3 of 20 mM phosphate buffer pH 7.2 (volume ratio = 1–1000) at 45 $^{\circ}\text{C}$ (using GeBAflex-tube 8kDa MWCO), and the mixture was extruded through 100 nm pore membrane 11 times at 45 $^{\circ}\text{C}$ using the LiposoFast instrument (Avanti polar lipids, Inc.)

Dynamic Light Scattering. Dynamic light scattering data were collected using the Zetasizer Nano ZS instrument (Malvern Instruments, Great Britain) operating at 25 $^{\circ}\text{C}$ with a laser wavelength λ of 620 nm and a scattering angle θ of 173 $^{\circ}$. Measurements were made using polystyrene low-volume microcuvettes (BrandTech Scientific, Inc. USA). Cuvettes were filled with 100 μL of vesicle dispersion for DLS characterization. DLS data is shown in Figure S1.

Cryo-EM Imaging. For the cryo-EM measurement, 3 μL of SUV/NP samples were loaded on a glow discharged (EmiTech K100 machine) Quantifoil grid or lacey grid that was blotted and plunged into liquid ethane using a Gatan CP3 automated plunger and stored in liquid nitrogen until use. Frozen specimens (samples with vesicles embedded in vitreous ice) were transferred to a Gatan 914 cryo-holder and maintained at temperatures below -176 $^{\circ}\text{C}$ inside the microscope. Samples were inspected with a Tecnai G2 microscope with an acceleration voltage of 120 kV, which is equipped with a cryobox decontaminator. Images were taken using a Digital Micrograph with a MultiScan Camera model 794 in different resolutions.

Data Analysis for Insertion Efficiency. The efficiency of NP-membrane incorporation was evaluated by calculation of the fraction

of NPs that inserted the SUV lipid membrane. Three different experiments were conducted for each condition for every NP except for the 7 nm NP with “native” membrane SUVs where only 2 experiments were made. The insertion efficiency was calculated as # membrane inserted NPs/total # NPs in a frame and the complementary noninserted NPs as # noninserted NPs/total # NPs in a frame. Error bars represent the standard deviation of the number of inserted or noninserted particles observed between repetitions of each vesicle preparation.

Simulation Methods. We used GROMACS 2021.5^{50,51} to perform all simulations using a leapfrog integrator with a time step of 20 fs. The MARTINI⁴¹ force field, version 2.3P,^{42,43} with the refined polarizable water model,⁴⁴ was used to model the interactions. Energy minimization, equilibration, and production simulation parameters were the same for all of the systems. Energy minimization was performed for 5,000 steps or until the maximum force was below 1,000 kJ/mol·nm. System equilibration and production runs were performed in the NPT ensemble. The temperature was controlled at 300 K using a velocity-rescale thermostat with a time constant of 1 ps. During equilibration runs, the pressure was controlled at 1 bar using the Berendsen barostat with semi-isotropic pressure coupling with a time constant of 5 ps and compressibility of 3×10^{-4} bar⁻¹. A 5 ns equilibration was performed with a time step of 10 fs, followed by a 15 ns equilibration with a time step of 15 fs, and a final 25 ns equilibration with a time step of 20 fs, for a total of 45 ns of equilibration. Production runs were performed using the same parameters as the equilibration runs with the exception of the barostat, which was switched to a Parrinello–Rahman barostat with a time constant of 12 ps. We used the Visual Molecular Dynamics (VMD)⁵² software, release 1.9.4a55, to generate all simulation snapshots.

System Setup for Coarse-Grained MD Simulations. We modeled the 5, 7, and 11 nm spherical CdSe/ZnS QDs as hollow shells coated with hydrophobic octadecylamine ligands. We coated the QD surface at a grafting density of 3.9 ligands/nm² based on the literature of similar CdSe/ZnS QDs.^{53–55} Details on the coarse-grained models⁵⁷ are included in the Supporting Information (Figure S4 and Table S3).

Lipids were modeled according to their standard topologies in MARTINI with PC24 modeled as DNPC. The MARTINI topology for DOTAP was added to this script. All bilayer lipid mixtures were generated using the insane.py script.⁵⁶ Pure (i.e., without inserted QDs) native and thick bilayers were simulated in $15 \times 15 \times 10$ nm simulation boxes for 100 ns to quantify their bulk properties; the last 50 ns were used for analyses (Figure S9). For the QD/bilayer systems, the QD was placed in the middle of the bilayer and solvated with polarizable water. We neutralized the system by adding a number of Cl⁻ ions equal to the number of DOTAP lipids using the gmx genion tool. The box size was $36 \times 36 \times 16$ nm for the 5 nm QD, $38 \times 38 \times 16$ nm for the 7 nm QD, and $42 \times 42 \times 20$ nm for the 11 nm QD. We specified an initial area per lipid of 0.7 nm²/lipid to ensure system stability. The total numbers of molecules for all systems are listed in Table S4 and Table S5.

We performed production simulations of 200 ns for the systems with the 5 and 7 nm QDs and 400 ns for the system with the 11 nm QD, sampling every 0.2 ns. System convergence was assessed by plotting the area per lipid (nm²) throughout the production run (Figure S5). As the QD size increases, longer equilibration times were required. The last 100 ns of simulation time for all QD/bilayer systems were deemed as converged and used for subsequent analyses.

■ ASSOCIATED CONTENT

51 Supporting Information

The Supporting Information is available free of charge at <https://pubs.acs.org/doi/10.1021/acs.langmuir.3c03471>.

DLS data, NP characteristics, SUV/NP preparation components, parameters of the coarse-grained model, additional simulation methods, number of molecules for

each QD/bilayer system, and simulation snapshots (PDF)

■ AUTHOR INFORMATION

Corresponding Authors

Asaf Grupi – Institute for Nanotechnology and Advanced Materials, Bar-Ilan University, Ramat-Gan 52900, Israel; Department of Physics, Bar-Ilan University, Ramat-Gan 52900, Israel; Email: grupia@gmail.com

Reid C. Van Lehn – Department of Chemical and Biological Engineering, University of Wisconsin – Madison, Madison, Wisconsin 53706, United States; Department of Chemistry, University of Wisconsin – Madison, Madison, Wisconsin 53706, United States; orcid.org/0000-0003-4885-6599; Email: vanlehn@wisc.edu

Shimon Weiss – Institute for Nanotechnology and Advanced Materials, Bar-Ilan University, Ramat-Gan 52900, Israel; Department of Physics, Bar-Ilan University, Ramat-Gan 52900, Israel; Department of Chemistry and Biochemistry and California NanoSystems Institute, University of California Los Angeles, Los Angeles, California 90095, United States; orcid.org/0000-0002-0720-5426; Email: sweiss@chem.ucla.edu

Authors

Adan Marzouq – Department of Chemistry, Bar-Ilan University, Ramat-Gan 52900, Israel; Institute for Nanotechnology and Advanced Materials, Bar-Ilan University, Ramat-Gan 52900, Israel

Lion Morgenstein – Institute for Nanotechnology and Advanced Materials, Bar-Ilan University, Ramat-Gan 52900, Israel; Department of Physics, Bar-Ilan University, Ramat-Gan 52900, Israel; Azrieli Faculty of Medicine, Bar-Ilan University, Safed 1311502, Israel; orcid.org/0000-0002-6190-421X

Carlos A. Huang-Zhu – Department of Chemical and Biological Engineering, University of Wisconsin – Madison, Madison, Wisconsin 53706, United States; orcid.org/0000-0002-4467-6462

Shimon Yudovich – Institute for Nanotechnology and Advanced Materials, Bar-Ilan University, Ramat-Gan 52900, Israel; Department of Physics, Bar-Ilan University, Ramat-Gan 52900, Israel; Department of Molecular and Cell Biology, University of California, Berkeley, California 94720, United States

Ayelet Atkins – Institute for Nanotechnology and Advanced Materials, Bar-Ilan University, Ramat-Gan 52900, Israel; orcid.org/0000-0001-9060-9298

Complete contact information is available at: <https://pubs.acs.org/doi/10.1021/acs.langmuir.3c03471>

Author Contributions

[¶]A.M., L.M., and C.A.H.Z. contributed equally to this work.

Notes

The authors declare no competing financial interest.

■ ACKNOWLEDGMENTS

This work has received funding from the European Research Council (ERC) under the European Union's Horizon 2020 research and innovation program under grant agreement no. 669941 and ERC-POC grant agreement no. 779896, the BER program of the Department of Energy Office of Science grant

DE-SC0020338, the STROBE National Science Foundation Science & Technology Center, grant no. DMR-1548924, the Israel Science Foundation grant # 813/19, and the Bar-Ilan Research & Development Co, the Israel Innovation Authority, grant no. 63392. C.A.H.Z and R.C.V. acknowledge the support provided by the Graduate Engineering Research Scholars – Advanced Opportunity Fellowship from the University of Wisconsin – Madison, the National Institute of General Medical Sciences' Chemistry-Biology Interface Training Program (5T32GM008505-29) from the University of Wisconsin – Madison, and from the National Science Foundation CAREER Award no. DMR-2044997. This work used the Advanced Cyberinfrastructure Coordination Ecosystem: Services & Support (ACCESS), which is supported by the National Science Foundation under Grant no. 2138307.

REFERENCES

- (1) Peng, Z. A.; Peng, X. Nearly Monodisperse and Shape-Controlled CdSe Nanocrystals via Alternative Routes: Nucleation and Growth. *J. Am. Chem. Soc.* **2002**, *124* (13), 3343–3353.
- (2) Peng, X.; Manna, L.; Yang, W.; Wickham, J.; Scher, E.; Kadavanich, A.; Alivisatos, A. P. Shape Control of CdSe Nanocrystals. *Nature* **2000**, *404* (6773), 59–61.
- (3) Manna, L.; Scher, E. C.; Alivisatos, A. P. Synthesis of Soluble and Processable Rod-, Arrow-, Teardrop-, and Tetrapod-Shaped CdSe Nanocrystals. *J. Am. Chem. Soc.* **2000**, *122* (51), 12700–12706.
- (4) De Leo, V.; Catucci, L.; Falqui, A.; Marotta, R.; Striccoli, M.; Agostiano, A.; Comparelli, R.; Milano, F. Hybrid Assemblies of Fluorescent Nanocrystals and Membrane Proteins in Liposomes. *Langmuir* **2014**, *30* (6), 1599–1608.
- (5) Hewa-Kasakarage, N. N.; Kirsanova, M.; Nemchinov, A.; Schmall, N.; El-Khoury, P. Z.; Tarnovsky, A. N.; Zamkov, M. Radiative Recombination of Spatially Extended Excitons in (ZnSe/CdS)/CdS Heterostructured Nanorods. *J. Am. Chem. Soc.* **2009**, *131* (3), 1328–1334.
- (6) Müller, J.; Lupton, J. M.; Rogach, A. L.; Feldmann, J.; Talapin, D. V.; Weller, H. Monitoring Surface Charge Migration in the Spectral Dynamics of Single CdSe CdS Nanodot/Nanorod Heterostructures. *Phys. Rev. B* **2005**, *72* (20), 205339.
- (7) Talapin, D. V.; Nelson, J. H.; Shevchenko, E. V.; Aloni, S.; Sadtler, B.; Alivisatos, A. P. Seeded Growth of Highly Luminescent CdSe/CdS Nanoheterostructures with Rod and Tetrapod Morphologies. *Nano Lett.* **2007**, *7* (10), 2951–2959.
- (8) Müller, J.; Lupton, J. M.; Lagoudakis, P. G.; Schindler, F.; Koeppe, R.; Rogach, A. L.; Feldmann, J.; Talapin, D. V.; Weller, H. Wave Function Engineering in Elongated Semiconductor Nanocrystals with Heterogeneous Carrier Confinement. *Nano Lett.* **2005**, *5* (10), 2044–2049.
- (9) Kim, T. H.; Cho, K. S.; Lee, E. K.; Lee, S. J.; Chae, J.; Kim, J. W.; Kim, D. H.; Kwon, J. Y.; Amaratunga, G.; Lee, S. Y.; et al. Full-Colour Quantum Dot Displays Fabricated by Transfer Printing. *Nat. Photonics* **2011**, *5* (3), 176–182.
- (10) Klimov, V. I.; Ivanov, S. A.; Nanda, J.; Achermann, M.; Bezel, I.; McGuire, J. A.; Piryatinski, A. Single-Exciton Optical Gain in Semiconductor Nanocrystals. *Nature* **2007**, *447* (7143), 441–446.
- (11) Michalet, X.; Pinaud, F. F.; Bentolila, L. A.; Tsay, J. M.; Doose, S.; Li, J. J.; Sundaresan, G.; Wu, A. M.; Gambhir, S. S.; Weiss, S. Quantum Dots for Live Cells, in Vivo Imaging, and Diagnostics. *Science* **2005**, *307* (5709), 538–544.
- (12) Li, S.; Zhang, K.; Yang, J. M.; Lin, L.; Yang, H. Single Quantum Dots as Local Temperature Markers. *Nano Lett.* **2007**, *7* (10), 3102–3105.
- (13) Ruedas-Rama, M. J.; Hall, E. A. H. Azamacrocyclic Activated Quantum Dot for Zinc Ion Detection. *Anal. Chem.* **2008**, *80* (21), 8260–8268.
- (14) Aouani, H.; Itzhakov, S.; Gachet, D.; Devaux, E.; Ebbesen, T. W.; Rigneault, H.; Oron, D.; Wenger, J. Colloidal Quantum Dots as Probes of Excitation Field Enhancement in Photonic Antennas. *ACS Nano* **2010**, *4* (8), 4571–4578.
- (15) Zhu, H.; Song, N.; Lv, H.; Hill, C. L.; Lian, T. Near Unity Quantum Yield of Light-Driven Redox Mediator Reduction and Efficient H₂ Generation Using Colloidal Nanorod Heterostructures. *J. Am. Chem. Soc.* **2012**, *134* (28), 11701–11708.
- (16) Mora-Seró, L.; Bisquert, J. Breakthroughs in the Development of Semiconductor-Sensitized Solar Cells. *J. Phys. Chem. Lett.* **2010**, *1* (20), 3046–3052.
- (17) Fakhruddin, R. F.; Zamaleeva, A. I.; Minullina, R. T.; Konnova, S. A.; Paunov, V. N. Cyborg Cells: Functionalisation of Living Cells with Polymers and Nanomaterials. *Chem. Soc. Rev.* **2012**, *41* (11), 4189–4206.
- (18) Wang, J. Z.; Ding, Z. Q.; Zhang, F.; Ye, W. B. Recent Development in Cell Encapsulations and Their Therapeutic Applications. *Mater. Sci. Eng.* **2017**, *77*, 1247–1260.
- (19) Kim, B. J.; Cho, H.; Park, J. H.; Mano, J. F.; Choi, I. S. Strategic Advances in Formation of Cell-in-Shell Structures: From Syntheses to Applications. *Adv. Mater.* **2018**, *30* (14), 1706063.
- (20) Liu, T.; Wang, Y.; Zhong, W.; Li, B.; Mequanint, K.; Luo, G.; Xing, M. Biomedical Applications of Layer-by-Layer Self-Assembly for Cell Encapsulation: Current Status and Future Perspectives. *Adv. Healthcare Mater.* **2019**, *8* (1), 1800939.
- (21) Van Lehn, R. C.; Atukorale, P. U.; Carney, R. P.; Yang, Y. S.; Stellacci, F.; Irvine, D. J.; Alexander-Katz, A. Effect of Particle Diameter and Surface Composition on the Spontaneous Fusion of Monolayer-Protected Gold Nanoparticles with Lipid Bilayers. *Nano Lett.* **2013**, *13* (9), 4060–4067.
- (22) Pandey, P.; Singh, S. P.; Arya, S. K.; Gupta, V.; Datta, M.; Singh, S.; Malhotra, B. D. Application of Thiolated Gold Nanoparticles for the Enhancement of Glucose Oxidase Activity. *Langmuir* **2007**, *23* (6), 3333–3337.
- (23) Tikhomirov, G.; Hoogland, S.; Lee, P. E.; Fischer, A.; Sargent, E. H.; Kelley, S. O. DNA-Based Programming of Quantum Dot Valency, Self-Assembly and Luminescence. *Nature* **2011**, *6* (8), 485–490.
- (24) Åkerman, M. E.; Chan, W. C. W.; Laakkonen, P.; Bhatia, S. N.; Ruoslahti, E. Nanocrystal Targeting in Vivo. *Proc. Natl. Acad. Sci. U. S. A.* **2002**, *99* (20), 12617–12621.
- (25) Derfus, A. M.; Chan, W. C. W.; Bhatia, S. N. Intracellular Delivery of Quantum Dots for Live Cell Labeling and Organelle Tracking. *Adv. Mater.* **2004**, *16* (12), 961–966.
- (26) Cathcart, K.; Patel, A.; Dies, H.; Rheinstädter, M. C.; Fradin, C. Effect of Cholesterol on the Structure of a Five-Component Mitochondria-Like Phospholipid Membrane. *Membranes* **2015**, *5* (4), 664–684.
- (27) Tharad, S.; Üzülmöz, Ö.; Promdonkoy, B.; Toca-Herrera, J. L. Cholesterol Increases Lipid Binding Rate and Changes Binding Behavior of Bacillus Thuringiensis Cytolytic Protein. *Int. J. Mol. Sci.* **2018**, *19* (12), 3819.
- (28) De Leo, V.; Milano, F.; Paiano, A.; Bramato, R.; Giotta, L.; Comparelli, R.; Ruscigno, S.; Agostiano, A.; Bucci, C.; Catucci, L. Luminescent CdSe@ZnS Nanocrystals Embedded in Liposomes: A Cytotoxicity Study in HeLa Cells. *Toxicol Res.* **2017**, *6* (6), 947–957.
- (29) Gopalakrishnan, G.; Danelon, C.; Izewska, P.; Prummer, M.; Bolinger, P. Y.; Geissbühler, I.; Demurtas, D.; Dubochet, J.; Vogel, H. Multifunctional Lipid/Quantum Dot Hybrid Nanocapsules for Controlled Targeting of Live Cells. *Angew. Chem., Int. Ed.* **2006**, *45* (33), 5478–5483.
- (30) Guo, X.; Zhang, Y.; Liu, J.; Yang, X.; Huang, J.; Li, L.; Wan, L.; Wang, K. Red Blood Cell Membrane-Mediated Fusion of Hydrophobic Quantum Dots with Living Cell Membranes for Cell Imaging. *J. Mater. Chem. B* **2016**, *4* (23), 4191–4197.
- (31) Van Lehn, R. C.; Alexander-Katz, A. Membrane-Embedded Nanoparticles Induce Lipid Rearrangements Similar to Those Exhibited by Biological Membrane Proteins. *J. Phys. Chem. B* **2014**, *118* (44), 12586–12598.
- (32) Lorent, J. H.; Diaz-Rohrer, B.; Lin, X.; Spring, K.; Gofe, A. A.; Levental, K. R.; Levental, I. Structural Determinants and Functional

- Consequences of Protein Affinity for Membrane Rafts. *Nat. Commun.* **2017**, *8* (1), 1219.
- (33) Mouritsen, O. G.; Bloom, M. Mattress Model of Lipid-Protein Interactions in Membranes. *Biophys. J.* **1984**, *46* (2), 141–153.
- (34) Lazzarini, A.; Macchiarulo, A.; Floridi, A.; Coletti, A.; Cataldi, S.; Codini, M.; Lazzarini, R.; Bartoccini, E.; Cascianelli, G.; Ambesi-Impiombato, F. S.; et al. Very-Long-Chain Fatty Acid Sphingomyelin in Nuclear Lipid Microdomains of Hepatocytes and Hepatoma Cells: Can the Exchange from C24: 0 to C16: 0 Affect Signal Proteins and Vitamin D Receptor? *Mol. Biol. Cell* **2015**, *26* (13), 2418–2425.
- (35) Courtney, K. C.; Pezeshkian, W.; Raghupathy, R.; Zhang, C.; Darbyson, A.; Ipsen, J. H.; Ford, D. A.; Khandelia, H.; Presley, J. F.; Zha, X. C24 Sphingolipids Govern the Transbilayer Asymmetry of Cholesterol and Lateral Organization of Model and Live-Cell Plasma Membranes. *Cell Rep.* **2018**, *24* (4), 1037–1049.
- (36) Zhang, H. Thin-Film Hydration Followed by Extrusion Method for Liposome Preparation. In *Methods in Molecular Biology*; Humana Press Inc; 2017, Vol. 1522, pp. 1722.
- (37) Schwendener, R. A. Liposomes as Vaccine Delivery Systems: A Review of the Recent Advances. *Ther. Adv. Vaccines* **2014**, *2* (6), 159–182.
- (38) Metso, A. J.; Zhao, H.; Tuunainen, I.; Kinnunen, P. K. J. Observation of the Main Phase Transition of Dinervonoylphosphocholine Giant Liposomes by Fluorescence Microscopy. *Biochim. Biophys. Acta, Biomembr.* **2005**, *1713* (2), 83–91.
- (39) Reviakine, I.; Gallego, M.; Johannsmann, D.; Tellechea, E. Adsorbed Liposome Deformation Studied with Quartz Crystal Microbalance. *J. Chem. Phys.* **2012**, *136* (8), 84702.
- (40) Adan, A.; Lion, M.; Huang-Zhu, C. A.; Yudovich, S.; Ayelet, A.; Asaf, G.; Van Lehn, R. C.; Shimon, W. Long-chain lipids facilitate insertion of large nanoparticles into membranes of small unilamellar vesicles. *bioRxiv* **2024**.
- (41) Marrink, S. J.; Risselada, H. J.; Yefimov, S.; Tieleman, D. P.; De Vries, A. H. The MARTINI Force Field: Coarse Grained Model for Biomolecular Simulations. *J. Phys. Chem. B* **2007**, *111* (27), 7812–7824.
- (42) Khan, H. M.; Souza, P. C. T.; Thallmair, S.; Barnoud, J.; De Vries, A. H.; Marrink, S. J.; Reuter, N. Capturing Choline-Aromatics Cation- π Interactions in the MARTINI Force Field. *J. Chem. Theory Comput.* **2020**, *16* (4), 2550–2560.
- (43) De Jong, D. H.; Singh, G.; Bennett, W. F. D.; Arnarez, C.; Wassenaar, T. A.; Schäfer, L. V.; Periole, X.; Tieleman, D. P.; Marrink, S. J. Improved Parameters for the Martini Coarse-Grained Protein Force Field. *J. Chem. Theory Comput.* **2013**, *9* (1), 687–697.
- (44) Michalowsky, J.; Schäfer, L. V.; Holm, C.; Smiatek, J. A Refined Polarizable Water Model for the Coarse-Grained MARTINI Force Field with Long-Range Electrostatic Interactions. *J. Chem. Phys.* **2017**, *146* (5), 054501.
- (45) Gkeka, P.; Angelikopoulos, P.; Sarkisov, L.; Cournia, Z. Membrane Partitioning of Anionic, Ligand-Coated Nanoparticles Is Accompanied by Ligand Snorkeling, Local Disordering, and Cholesterol Depletion. *PLoS Comput. Biol.* **2014**, *10* (12), No. e1003917.
- (46) Lolicato, F.; Joly, L.; Martinez-Seara, H.; Fragneto, G.; Scoppola, E.; Baldelli Bombelli, F.; Vattulainen, I.; Akola, J.; Maccarini, M. The Role of Temperature and Lipid Charge on Intake/Uptake of Cationic Gold Nanoparticles into Lipid Bilayers. *Small* **2019**, *15* (23), 1805046.
- (47) Chew, A. K.; Van Lehn, R. C. Effect of Core Morphology on the Structural Asymmetry of Alkanethiol Monolayer-Protected Gold Nanoparticles. *J. Phys. Chem. C* **2018**, *122* (45), 26288–26297.
- (48) Piggot, T. J.; Allison, J. R.; Sessions, R. B.; Essex, J. W. On the Calculation of Acyl Chain Order Parameters from Lipid Simulations. *J. Chem. Theory Comput.* **2017**, *13* (11), 5683–5696.
- (49) Trabelsi, S.; Zhang, S.; Lee, T. R.; Schwartz, D. K. Linactants: Surfactant Analogues in Two Dimensions. *Phys. Rev. Lett.* **2008**, *100* (3), 037802.
- (50) Van Der Spoel, D.; Lindahl, E.; Hess, B.; Groenhof, G.; Mark, A. E.; Berendsen, H. J. C. GROMACS: Fast, Flexible, and Free. *J. Comput. Chem.* **2005**, *26* (16), 1701–1718.
- (51) Lindahl, E.; Abraham, M. J.; Hess, B.; van der Spoel, D.; GROMACS 2021.5 Source code, Zenodo, 2022.
- (52) Humphrey, W.; Dalke, A.; Schulten, K. VMD: Visual Molecular Dynamics. *J. Mol. Graphics* **1996**, *14* (1), 33–38.
- (53) Watson, B. R.; Ma, Y. Z.; Cahill, J. F.; Doughty, B.; Calhoun, T. R. Probing Ligand Removal and Ordering at Quantum Dot Surfaces Using Vibrational Sum Frequency Generation Spectroscopy. *J. Colloid Interface Sci.* **2019**, *537*, 389–395.
- (54) Turo, M. J.; Shen, X.; Brandon, N. K.; Castillo, S.; Fall, A. M.; Pantelides, S. T.; Macdonald, J. E. Dual-Mode Crystal-Bound and X-Type Passivation of Quantum Dots. *Chem. Commun.* **2016**, *52* (82), 12214–12217.
- (55) Dunlap, J. H.; Jayaweera, N. P.; Pellechia, P. J.; Greytak, A. B. Competitive Anionic Exchange of Thiolate Ligands onto Aqueous Phosphonate-Capped Quantum Dots. *J. Phys. Chem. C* **2022**, *126* (41), 17635–17646.
- (56) Wassenaar, T. A.; Ingólfsson, H. I.; Böckmann, R. A.; Tieleman, D. P.; Marrink, S. J. Computational Lipidomics with Insane: A Versatile Tool for Generating Custom Membranes for Molecular Simulations. *J. Chem. Theory Comput.* **2015**, *11* (5), 2144–2155.
- (57) Huang-Zhu, C. A.; Sheavly, J. K.; Chew, A. K.; Patel, S. J.; Van Lehn, R. C. Ligand Lipophilicity Determines Molecular Mechanisms of Nanoparticle Adsorption to Lipid Bilayers. *ACS Nano* **2024**, *18* (8), 6424–6437.